INTERNATIONAL JOURNAL FOR NUMERICAL METHODS IN FLUIDS, VOL. 8, 1071–1093 (1988)

WAVE EQUATION HYDRODYNAMICS ON DEFORMING ELEMENTS

GUNNAR L. D. SIDÉN AND DANIEL R. LYNCH
Thayer School of Engineering, Dartmouth College, Hanover, NH 03755, U.S.A.

SUMMARY

The shallow water wave equation is derived in a general deforming co-ordinate system. A weak form is developed which displays the natural boundary condition prominently and which may be implemented on C^0 elements. A time-stepping algorithm is implemented with elastic mapping of interior node motion. Lossless test cases show agreement with analytic solutions. A simple hypothetical test case shows intuitively good behaviour at length scales approaching those required of estuarine simulations.

KEY WORDS Finite Element Deforming Element Moving Boundary Shallow Water Hydrodynamics

INTRODUCTION

In this paper we develop solutions to the shallow water equations with moving boundaries for problems approaching estuarine length scales. The basic deforming element approach follows that introduced previously[1] and capitalizes on the geometric suitability of finite elements for front-tracking simulations. The original paper presented a few example solutions to show the promise of the method, at length scales appropriate to storm surge calculations. The relatively small boundary excursions in these examples were resolvable by moving only the boundary nodes, keeping interior nodes fixed.

Because of the difficulties inherent in numerical fluid mechanics, we have since pursued the development of deforming element ideas in simpler diffusion situations, for three reasons:

(a) There are several physically important problems in heat transfer with phase change.
(b) The numerical point of departure—diffusion on a fixed mesh—is well understood, allowing us to focus on the deforming element extension *per se*.
(c) Very large mesh deformations are required to solve problems of practical interest in this area.

A series of investigations, culminating in the simulation of physically unstable interface shapes during crystal growth, has shown that very large, complex mesh deformations may be accurately accomodated.[2–5] These findings complement those of several others.[6–10] As a result of these lines of development, we are confident in our ability to construct accurate simulations on deforming elements.

A parallel effort has been devoted to finite element solution of fixed boundary, shallow water problems in the context of tidal hydrodynamics. The approach here employs the shallow water wave equation in place of the primitive continuity equation.[11] This was originally developed to

0271–2091/88/091071–23$11.50

Received 1 June 1987
Revised 1 January 1988

overcome short-wavelength parasitic modes which appear in many primitive equation models; fortuitously it also provides several important computational economies as well. The original model, with modifications by Kinnmark and Gray,[12,13] has now been successfully tested against field observations.[14-17] Tidal simulations of up to 190 (simulated) days have been performed on a microcomputer.[18] As a result of these studies, we are confident in our ability to simulate tidal hydrodynamics on fixed finite elements.

The present paper incorporates both lines of development. Extension of the original work toward estuarine length scales demands smaller elements and larger relative deformations, with all interior elements deforming. We begin by deriving the shallow water wave equation in a general deforming co-ordinate system, and produce a weak form which is compatible with simple C^0 elements and which displays the natural conditions on the moving boundary. Utilizing elastic mappings to manage interior node motion, we show comparisons with two analytic solutions plus two simple illustrative estuarine problems.

The objective of simulating detailed estuarine circulation demands that increased attention be paid to advective instabilities. We address these here by simply making the advective momentum terms implicit. We recognize, however, that this is an interim solution to a fundamental problem which needs a more comprehensive and cost-effective solution.

GOVERNING EQUATIONS AND DISCRETIZATION

The governing equations are the shallow water equations obtained by vertically averaging the continuity and momentum equations for a homogenous hydrostatic fluid. In primitive form they are:

continuity

$$\partial H/\partial t+\nabla\cdot H\mathbf{v}=0, \tag{1}$$

momentum

$$\partial H\mathbf{v}/\partial t+\nabla\cdot(H\mathbf{v}\mathbf{v})+gH\nabla\zeta+\mathbf{f}\times H\mathbf{v}+\tau H\mathbf{v}=H\mathbf{\Psi}, \tag{2}$$

where $H(x, y, t)$ is the total fluid depth, $\zeta(x, y, t)$ is the elevation of the free surface above mean sea level, $h(x, y)$ is the bathymetry ($h=H-\zeta$), $\mathbf{v}(x, y, t)$ is the vertically averaged horizontal fluid velocity, g is the acceleration due to gravity, $\mathbf{f}$ is the vector Coriolis parameter, $\tau(x, y, t)$ is the bottom friction parameter, $\mathbf{\Psi}$ accounts for momentum input at the surface (such as wind stress), x is positive eastward, y is positive northward, t is time and ∇ is the gradient operator. Consistent with the 'shallow' scaling assumptions, we neglect horizontal shear stresses but include the effect of vertical shear in the bottom stress term $\tau H\mathbf{v}$.

We first introduce the total time derivative

$$\mathrm{d}/\mathrm{d}t=\partial/\partial t+\mathbf{v}^{\mathrm{e}}\cdot\nabla \tag{3}$$

in order to express the equations in the co-ordinate system attached to an arbitrary motion $\mathbf{v}^{\mathrm{e}}\neq\mathbf{v}$:

continuity

$$\mathrm{d}H/\mathrm{d}t-\mathbf{v}^{\mathrm{e}}\cdot\nabla H+\nabla\cdot H\mathbf{v}=0 \tag{4}$$

or equivalently

$$\mathrm{d}H/\mathrm{d}t+\nabla\cdot H(\mathbf{v}-\mathbf{v}^{\mathrm{e}})+H\nabla\cdot\mathbf{v}^{\mathrm{e}}=0, \tag{5}$$

momentum

$$\mathrm{d}H\mathbf{v}/\mathrm{d}t-\mathbf{v}^{\mathrm{e}}\cdot\nabla H\mathbf{v}+\nabla\cdot(H\mathbf{v}\mathbf{v})+gH\nabla\zeta+\mathbf{f}\times H\mathbf{v}+\tau H\mathbf{v}=H\boldsymbol{\Psi}. \tag{6}$$

Substitution of (4) into (6) then yields the alternative form of the momentum equation:

$$\mathrm{d}\mathbf{v}/\mathrm{d}t+(\mathbf{v}-\mathbf{v}^{\mathrm{e}})\cdot\nabla\mathbf{v}+g\nabla\zeta+\mathbf{f}\times\mathbf{v}+\tau\mathbf{v}=\boldsymbol{\Psi}. \tag{7}$$

The shallow water wave equation is obtained by operating on the continuity equation (5) and the momentum equation (6). Here we follow the derivations of Lynch and Gray[11] and Kinnmark and Gray,[12, 13] focusing on the additional terms that arise due to the deformation of the grid. *En route* we employ the two less common identities which are derived in the Appendix:

$$\frac{\mathrm{d}}{\mathrm{d}t}\nabla=\nabla\frac{\mathrm{d}}{\mathrm{d}t}-\nabla\mathbf{v}^{\mathrm{e}}\cdot\nabla, \tag{8a}$$

$$\frac{\mathrm{d}}{\mathrm{d}t}\nabla\cdot=\nabla\cdot\frac{\mathrm{d}}{\mathrm{d}t}-\nabla\mathbf{v}^{\mathrm{e}}:\nabla, \tag{8b}$$

where : denotes a scalar product between two tensors. Taking the total time derivative of the continuity equation (5) yields

$$\frac{\mathrm{d}^2H}{\mathrm{d}t^2}+\nabla\cdot\frac{\mathrm{d}H(\mathbf{v}-\mathbf{v}^{\mathrm{e}})}{\mathrm{d}t}-\nabla\mathbf{v}^{\mathrm{e}}:\nabla H(\mathbf{v}-\mathbf{v}^{\mathrm{e}})+\frac{\mathrm{d}H}{\mathrm{d}t}\nabla\cdot\mathbf{v}^{\mathrm{e}}+H\nabla\cdot\frac{\mathrm{d}\mathbf{v}^{\mathrm{e}}}{\mathrm{d}t}-H\nabla\mathbf{v}^{\mathrm{e}}:\nabla\mathbf{v}^{\mathrm{e}}=0, \tag{9}$$

which may be simplified to

$$\frac{\mathrm{d}^2H}{\mathrm{d}t^2}+\nabla\cdot\frac{\mathrm{d}H(\mathbf{v}-\mathbf{v}^{\mathrm{e}})}{\mathrm{d}t}+\frac{\mathrm{d}H}{\mathrm{d}t}\nabla\cdot\mathbf{v}^{\mathrm{e}}+H\nabla\cdot\frac{\mathrm{d}\mathbf{v}^{\mathrm{e}}}{\mathrm{d}t}+\mathbf{v}^{\mathrm{e}}\cdot\nabla\mathbf{v}^{\mathrm{e}}\cdot\nabla H-\nabla\mathbf{v}^{\mathrm{e}}:\nabla H\mathbf{v}=0. \tag{10}$$

We now obtain the weak form of (5) by requiring its orthogonality to a set of weighting functions ϕ_i:

$$\left\langle\frac{\mathrm{d}H}{\mathrm{d}t},\phi_i\right\rangle-\langle H(\mathbf{v}-\mathbf{v}^{\mathrm{e}}),\nabla\phi_i\rangle+\langle H\nabla\cdot\mathbf{v}^{\mathrm{e}},\phi_i\rangle=-\oint H(\mathbf{v}-\mathbf{v}^{\mathrm{e}})\cdot\mathbf{n}\phi_i\,\mathrm{d}s, \tag{11}$$

where $\langle\ \rangle$ denotes the inner product

$$\langle a,b\rangle=\iint a\cdot b\,\mathrm{d}x\,\mathrm{d}y. \tag{12}$$

The line integral is evaluated along the boundary and $\mathbf{n}$ is the unit normal vector directed outwards. Note that we have purposely expressed the natural boundary condition $H(\mathbf{v}-\mathbf{v}^{\mathrm{e}})$ in this integral. In a similar manner we obtain the weak form of (10):

$$\left\langle\frac{\mathrm{d}^2H}{\mathrm{d}t^2},\phi_i\right\rangle-\left\langle\frac{\mathrm{d}H(\mathbf{v}-\mathbf{v}^{\mathrm{e}})}{\mathrm{d}t},\nabla\phi_i\right\rangle+\left\langle\frac{\mathrm{d}H}{\mathrm{d}t}\nabla\cdot\mathbf{v}^{\mathrm{e}},\phi_i\right\rangle+\left\langle H\nabla\cdot\frac{\mathrm{d}\mathbf{v}^{\mathrm{e}}}{\mathrm{d}t},\phi_i\right\rangle$$
$$+\langle\mathbf{v}^{\mathrm{e}}\cdot\nabla\mathbf{v}^{\mathrm{e}}\cdot\nabla H,\phi_i\rangle-\langle\nabla\mathbf{v}^{\mathrm{e}}:\nabla H\mathbf{v},\phi_i\rangle=-\oint\frac{\mathrm{d}H(\mathbf{v}-\mathbf{v}^{\mathrm{e}})}{\mathrm{d}t}\cdot\mathbf{n}\phi_i\,\mathrm{d}s. \tag{13}$$

Next, a composite weak form is obtained by adding (11) times a numerical weighting parameter τ_0 to (13):

$$\left\langle \frac{\mathrm{d}^2 H}{\mathrm{d}t^2}, \phi_i \right\rangle + \left\langle \tau_0 \frac{\mathrm{d}H}{\mathrm{d}t}, \phi_i \right\rangle - \left\langle \left[\frac{\mathrm{d}H(\mathbf{v}-\mathbf{v}^{\mathrm{e}})}{\mathrm{d}t} + \tau_0 H(\mathbf{v}-\mathbf{v}^{\mathrm{e}}) \right], \nabla\phi_i \right\rangle$$
$$+ \left\langle \frac{\mathrm{d}H}{\mathrm{d}t} \nabla \cdot \mathbf{v}^{\mathrm{e}}, \phi_i \right\rangle + \langle \tau_0 H \nabla \cdot \mathbf{v}^{\mathrm{e}}, \phi_i \rangle + \left\langle H \nabla \cdot \frac{\mathrm{d}\mathbf{v}^{\mathrm{e}}}{\mathrm{d}t}, \phi_i \right\rangle + \langle \mathbf{v}^{\mathrm{e}} \cdot \nabla \mathbf{v}^{\mathrm{e}} \cdot \nabla H, \phi_i \rangle$$
$$- \langle \nabla \mathbf{v}^{\mathrm{e}} : \nabla H \mathbf{v}, \phi_i \rangle = - \oint \left[\frac{\mathrm{d}H(\mathbf{v}-\mathbf{v}^{\mathrm{e}})}{\mathrm{d}t} + \tau_0 H(\mathbf{v}-\mathbf{v}^{\mathrm{e}}) \right] \cdot \mathbf{n} \phi_i \, \mathrm{d}s. \tag{14}$$

The numerical weighting parameter τ_0, here constant in space, was originally introduced by Kinnmark and Gray[13] in order to render the implicit wave equation time-stepping matrix stationary. In addition to this desirable property, we find that this modification stabilizes a low-frequency drift which develops in long-term simulations with the original[11] formulation.[16] The final weak form of the wave equation which we employ is obtained by introducing the momentum equation (5) into the third term in (14):

$$\left\langle \frac{\mathrm{d}^2 H}{\mathrm{d}t^2}, \phi_i \right\rangle + \left\langle \tau_0 \frac{\mathrm{d}H}{\mathrm{d}t}, \phi_i \right\rangle + \left\langle H \frac{\mathrm{d}\mathbf{v}^{\mathrm{e}}}{\mathrm{d}t}, \nabla\phi_i \right\rangle + \left\langle \frac{\mathrm{d}H}{\mathrm{d}t} \mathbf{v}^{\mathrm{e}}, \nabla\phi_i \right\rangle + \left\langle \frac{\mathrm{d}H}{\mathrm{d}t} \nabla \cdot \mathbf{v}^{\mathrm{e}}, \phi_i \right\rangle$$
$$+ \langle [-\mathbf{v}^{\mathrm{e}} \cdot \nabla H \mathbf{v} + \nabla \cdot H \mathbf{v}\mathbf{v} + gH \nabla \zeta + \mathbf{f} \times H \mathbf{v} + (\tau - \tau_0) H \mathbf{v} + \tau_0 H \mathbf{v}^{\mathrm{e}} - H \boldsymbol{\Psi}], \nabla \phi_i \rangle$$
$$+ \langle \tau_0 H \nabla \cdot \mathbf{v}^{\mathrm{e}}, \phi_i \rangle + \left\langle H \nabla \cdot \frac{\mathrm{d}\mathbf{v}^{\mathrm{e}}}{\mathrm{d}t}, \phi_i \right\rangle + \langle \mathbf{v}^{\mathrm{e}} \cdot \nabla \mathbf{v}^{\mathrm{e}} \cdot \nabla H, \phi_i \rangle - \langle \nabla \mathbf{v}^{\mathrm{e}} : \nabla H \mathbf{v}, \phi_i \rangle$$
$$= - \oint \left[\frac{\mathrm{d}H(\mathbf{v}-\mathbf{v}^{\mathrm{e}})}{\mathrm{d}t} + \tau_0 H(\mathbf{v}-\mathbf{v}^{\mathrm{e}}) \right] \cdot \mathbf{n} \phi_i \, \mathrm{d}s. \tag{15}$$

The weak form of the momentum equation (7) is similarly obtained in a standard weighted residual manner:

$$\left\langle \frac{\mathrm{d}\mathbf{v}}{\mathrm{d}t}, \phi_i \right\rangle + \langle (\mathbf{v}-\mathbf{v}^{\mathrm{e}}) \cdot \nabla \mathbf{v}, \phi_i \rangle + \langle g \nabla \zeta, \phi_i \rangle + \langle \mathbf{f} \times \mathbf{v}, \phi_i \rangle + \langle \tau \mathbf{v}, \phi_i \rangle = \langle \boldsymbol{\Psi}, \phi_i \rangle. \tag{16}$$

Note that (15) and (16) involve only first derivatives and thus may be implemented on simple C^0 finite elements.

In this study we solve equations (15) and (16) on a deforming finite element grid. With the equations expressed in total time derivatives we are now free to let $\mathbf{v}^{\mathrm{e}}$ track the motion of the grid:

$$\mathbf{v}^{\mathrm{e}} \equiv \sum_{i=1}^{N} \frac{\mathrm{d}\mathbf{x}_i}{\mathrm{d}t} \phi_i. \tag{17}$$

Here $\mathbf{x}_i$ is the location of node i, $\mathrm{d}\mathbf{x}_i/\mathrm{d}t$ is the velocity of node i, N is the number of nodes and ϕ_i is the finite element basis. Note that this formulation is a generalization of that presented by Lynch and Gray[11] and Kinnmark and Gray.[13, 14] This can most easily be seen by letting $\mathbf{v}^{\mathrm{e}}(x, y, t)$ equal zero everywhere and by letting τ_0 equal τ in the cases where the latter is constant.

The Galerkin finite element procedure is used in discretizing the spatial domain. The integration is carried out on linear elements and the integrals are evaluated with quadrature points coincident with the nodes (integral lumping). The variables used are approximated with a set of N

finite element basis functions ϕ_j, identical to the weighting functions:

$$H \approx \sum_{j=1}^{N} H_j \phi_j \tag{18}$$

and likewise for ζ, $\mathbf{v}$, h and τ. As a result, from (17) we have especially simple time derivatives:

$$\frac{\mathrm{d}^2 H}{\mathrm{d}t^2} \approx \sum_{j=1}^{N} \frac{\mathrm{d}^2 H_j}{\mathrm{d}t^2} \phi_j, \tag{19a}$$

$$\frac{\mathrm{d}H}{\mathrm{d}t} \approx \sum_{j=1}^{N} \frac{\mathrm{d}H_j}{\mathrm{d}t} \phi_j, \tag{19b}$$

$$\frac{\mathrm{d}\mathbf{v}}{\mathrm{d}t} \approx \sum_{j=1}^{N} \frac{\mathrm{d}\mathbf{v}_j}{\mathrm{d}t} \phi_j, \tag{19c}$$

$$\frac{\mathrm{d}\mathbf{v}^e}{\mathrm{d}t} \equiv \sum_{j=1}^{N} \frac{\mathrm{d}^2 \mathbf{x}_j}{\mathrm{d}t^2} \phi_j, \tag{19d}$$

i.e. the terms involving time derivatives of ϕ are not invoked here since they are already embedded in the equations.

A three-level finite difference scheme is used to discretize the wave equation in the time domain.[11] A second-order leapfrog approximation of the time derivative of H yields

$$\frac{\mathrm{d}H_j}{\mathrm{d}t} \approx \frac{H_j^{k+1} - H_j^{k-1}}{2\Delta t} = \frac{\Delta H_j}{2\Delta t}, \tag{20a}$$

where $\Delta H = H^{k+1} - H^{k-1}$, the superscript k denotes the time level and Δt is the time step. In the same way we can approximate the second time derivative of H using a centred finite difference expression:

$$\frac{\mathrm{d}^2 H_j}{\mathrm{d}t^2} \approx \frac{H_j^{k+1} - 2H_j^k + H_j^{k-1}}{\Delta t^2} = \frac{\Delta H_j}{\Delta t^2} - 2\frac{H_j^k}{\Delta t^2} + 2\frac{H_j^{k-1}}{\Delta t^2}. \tag{20b}$$

The element velocity $\mathbf{v}^e$ can be expressed as the total time derivative of the node locations:

$$\mathbf{v}_j^e = \frac{\mathrm{d}\mathbf{x}_j}{\mathrm{d}t} \approx \frac{\mathbf{x}_j^{k+1} - \mathbf{x}_j^{k-1}}{2\Delta t}, \tag{20c}$$

where $\mathbf{x}_j$ is the x, y co-ordinates of node j. Similarly we have for the element acceleration

$$\frac{\mathrm{d}^2 \mathbf{x}_j}{\mathrm{d}t^2} \approx \frac{\mathbf{x}_j^{k+1} - 2\mathbf{x}_j^k + \mathbf{x}_j^{k-1}}{\Delta t^2}. \tag{20d}$$

Furthermore, ϕ and its derivatives are evaluated using the grid at time level k:

$$\phi_i^k = \phi_i(\mathbf{x}^k). \tag{20e}$$

The remaining terms are centred at time level k. The gravity term in (15) may be treated implicitly while still centred in time by use of the time weighting parameter θ:

$$Z^k \approx \frac{\theta}{2}(Z^{k+1} + Z^{k-1}) + (1-\theta)Z^k = \frac{\theta}{2}\Delta Z + Z^k + \theta(Z^{k-1} - Z^k), \tag{20f}$$

where θ varies from 0 (completely explicit) to 1 (completely implicit).

Substitution of the approximations (17)–(20) into (15) yields the matrix equation

$$[A]^k\{\Delta H\}^k=\{RW\}^k, \tag{21a}$$

where

$$A_{ij}^k=\langle\phi_j,\phi_i\rangle^k+\frac{\Delta t}{2}\langle\tau_0\phi_j,\phi_i\rangle^k+\frac{\Delta t}{2}\langle\mathbf{v}^{\mathrm{e}}\phi_j,\nabla\phi_i\rangle^k+\frac{\Delta t}{2}\langle\phi_j\nabla\cdot\mathbf{v}^{\mathrm{e}},\phi_i\rangle^k+\frac{\theta}{2}\Delta t^2\langle gH\nabla\phi_j,\nabla\phi_i\rangle^k \tag{21b}$$

and

$$\begin{aligned}RW_i^k={}&-\Delta t^2\left\langle gH^k\left[\nabla\zeta^k+\theta\nabla(\zeta^{k-1}-\zeta^k)-\frac{\theta}{2}\nabla(h^{k+1}-h^{k-1})\right],\nabla\phi_i\right\rangle^k\\&+2\langle(H^k-H^{k-1}),\phi_i\rangle^k-\Delta t^2\left\langle H\frac{\mathrm{d}\mathbf{v}^{\mathrm{e}}}{\mathrm{d}t},\nabla\phi_i\right\rangle^k-\Delta t^2\langle\tau_0H\nabla\cdot\mathbf{v}^{\mathrm{e}},\phi_i\rangle^k\\&-\Delta t^2\left\langle H\nabla\cdot\frac{\mathrm{d}\mathbf{v}^{\mathrm{e}}}{\mathrm{d}t},\phi_i\right\rangle^k-\Delta t^2\langle\mathbf{v}^{\mathrm{e}}\cdot\nabla\mathbf{v}^{\mathrm{e}}\cdot\nabla H,\phi_i\rangle^k+\Delta t^2\langle\nabla\mathbf{v}^{\mathrm{e}}:\nabla H\mathbf{v},\phi_i\rangle^k\\&-\Delta t^2\langle[-\mathbf{v}^{\mathrm{e}}\cdot\nabla H\mathbf{v}+\nabla\cdot H\mathbf{v}\mathbf{v}+\mathbf{f}\times H\mathbf{v}+(\tau-\tau_0)H\mathbf{v}+\tau_0H\mathbf{v}^{\mathrm{e}}-H\boldsymbol{\Psi}],\nabla\phi_i\rangle^k\\&-\Delta t^2\oint\left[\frac{\mathrm{d}H(\mathbf{v}-\mathbf{v}^{\mathrm{e}})}{\mathrm{d}t}+\tau_0H(\mathbf{v}-\mathbf{v}^{\mathrm{e}})\right]^k\cdot\mathbf{n}^k\,\phi_i^k\,\mathrm{d}s.\end{aligned} \tag{21c}$$

In the discretization of the momentum equation (16) a two-level scheme is adopted, utilizing time levels k and $k+1$, which is centred at time level $k+1/2$. The total time derivative of the fluid velocity is approximated according to

$$\frac{\mathrm{d}\mathbf{v}_j}{\mathrm{d}t}\approx\frac{\mathbf{v}_j^{k+1}-\mathbf{v}_j^k}{\Delta t}=\frac{\Delta\mathbf{v}_j}{\Delta t}. \tag{22a}$$

Furthermore, the element velocity is approximated by

$$\mathbf{v}_j^{\mathrm{e}}\approx\frac{\mathbf{x}_j^{k+1}-\mathbf{x}_j^k}{\Delta t} \tag{22b}$$

and consequently ϕ and its derivatives, which change through time due to the grid deformation, are evaluated using the grid at time level $k+1/2$:

$$\phi_i^{k+1/2}=\phi_i(\mathbf{x}^{k+1/2}), \tag{22c}$$

where the notation $k+1/2$ corresponds to the average of the two levels k and $k+1$:

$$Z^{k+1/2}=\tfrac{1}{2}(Z^k+Z^{k+1}). \tag{22d}$$

The remaining terms are linearized and centred at time level $k+1/2$. The problems of main concern in this study are characterized by short length scales and potentially large fluid velocities. This makes the treatment of the advective term in the momentum equation crucial for numerical stability. An implicit treatment of the advective term has in this study proven to yield successful results:

$$\mathbf{v}^{k+1/2}\cdot\nabla\mathbf{v}^{k+1/2}\approx\tfrac{1}{2}\mathbf{v}^{k+1}\cdot\nabla\mathbf{v}^k+\tfrac{1}{2}\mathbf{v}^k\cdot\nabla\mathbf{v}^{k+1}. \tag{22e}$$

This scheme[19] is linearly implicit while still second-order correct in time.

By substituting the approximations (18), (19), (22) into (16), the momentum equation reduces to the following matrix equation:

$$[B]^k\{\delta\mathrm{v}\}^k=\{RM\}^k, \tag{23a}$$

where

$$\delta\mathrm{v}_{2i-1}=\Delta u_i=u_i^{k+1}-u_i^k, \tag{23b}$$

$$\delta\mathrm{v}_{2i}=\Delta v_i=v_i^{k+1}-v_i^k. \tag{23c}$$

Here u_i and v_i are the x and y components of the fluid velocity $\mathbf{v}$. Similarly we denote the components of the grid velocity by u^e and v^e and the vertical component of the Coriolis vector $\mathbf{f}$ is denoted by f. The momentum matrix takes the following form:

$$\begin{aligned}B^k_{2i-1\,2j-1}=&\left\langle \phi_j,\,\phi_i\left(1+\frac{\Delta t}{2}\tau^k+\frac{\Delta t}{2}\frac{\partial u^k}{\partial x}\right)\right\rangle^{k+1/2}\\&+\frac{\Delta t}{2}\left\langle (u^k-u^e)\frac{\partial\phi_j}{\partial x},\,\phi_i\right\rangle^{k+1/2}+\left\langle (v^k-v^e)\frac{\partial\phi_j}{\partial y},\,\phi_i\right\rangle^{k+1/2},\end{aligned} \tag{23d}$$

$$B^k_{2i-1\,2j}=\frac{\Delta t}{2}\left\langle \phi_j,\,\phi_i\left(\frac{\partial u^k}{\partial y}-f\right)\right\rangle^{k+1/2}, \tag{23e}$$

$$B^k_{2i\,2j-1}=\frac{\Delta t}{2}\left\langle \phi_j,\,\phi_i\left(\frac{\partial v^k}{\partial x}+f\right)\right\rangle^{k+1/2}, \tag{23f}$$

$$\begin{aligned}B^k_{2i\,2j}=&\left\langle \phi_j,\,\phi_i\left(1+\frac{\Delta t}{2}\tau^k+\frac{\Delta t}{2}\frac{\partial v^k}{\partial y}\right)\right\rangle^{k+1/2}\\&+\frac{\Delta t}{2}\left\langle (u^k-u^e)\frac{\partial\phi_j}{\partial x},\,\phi_i\right\rangle^{k+1/2}+\left\langle (v^k-v^e)\frac{\partial\phi_j}{\partial y},\,\phi_i\right\rangle^{k+1/2},\end{aligned} \tag{23g}$$

$$\begin{aligned}RM^k_{2i-1}=&-\Delta t\left\langle (u^k-u^e)\frac{\partial u^k}{\partial x},\,\phi_i\right\rangle^{k+1/2}-\Delta t\left\langle (v^k-v^e)\frac{\partial u^k}{\partial y},\,\phi_i\right\rangle^{k+1/2}-\Delta t\left\langle g\frac{\partial\zeta}{\partial x},\,\phi_i\right\rangle^{k+1/2}\\&+\Delta t\langle fv^k,\,\phi_i\rangle^{k+1/2}-\Delta t\langle\tau u^k,\,\phi_i\rangle^{k+1/2}+\Delta t\langle\Psi_x,\,\phi_i\rangle^{k+1/2},\end{aligned} \tag{23h}$$

$$\begin{aligned}RM^k_{2i}=&-\Delta t\left\langle (u^k-u^e)\frac{\partial v^k}{\partial x},\,\phi_i\right\rangle^{k+1/2}-\Delta t\left\langle (v^k-v^e)\frac{\partial v^k}{\partial y},\,\phi_i\right\rangle^{k+1/2}-\Delta t\left\langle g\frac{\partial\zeta}{\partial y},\,\phi_i\right\rangle^{k+1/2}\\&-\Delta t\langle fu^k,\,\phi_i\rangle^{k+1/2}-\Delta t\langle\tau v^k,\,\phi_i\rangle^{k+1/2}+\Delta t\langle\Psi_y,\,\phi_i\rangle^{k+1/2}.\end{aligned} \tag{23i}$$

BOUNDARY CONDITIONS AND NODE MOTION

On fixed boundaries we apply boundary conditions on H or $\mathbf{v}\cdot\mathbf{n}$ in the conventional way as follows. Where H is known we sacrifice the wave equation in favour of exact specification of H_j. Conditions on $\mathbf{v}\cdot\mathbf{n}$ are enforced directly by sacrificing the normal component of the momentum equation in favour of exact specification of $\mathbf{v}\cdot\mathbf{n}$; in addition, prescribed values of $\mathbf{v}\cdot\mathbf{n}$ are used to evaluate the boundary integral in the wave equation. The local normal is computed to be parallel to $\oint\mathbf{n}\phi_i\mathrm{d}s$.[11]

On the moving boundary we have both $H=0$ and $(\mathbf{v}-\mathbf{v}^e)\cdot\mathbf{n}=0$. We satisfy $H=0$ exactly and sacrifice the wave equation there. The momentum equation is utilized to compute both components of $\mathbf{v}$, following which we set $(\mathbf{v}-\mathbf{v}^e)\cdot\mathbf{n}=0$ and $\mathbf{v}^e\cdot\mathbf{t}=0$.

On the interior $\mathbf{v}^e$ may be selected arbitrarily, consistent with good discretization practice and its known boundary values. In this work interior node positions are determined as the deformation response of an elastic medium in plane stress[3] with known boundary deformations. This permits the mesh topology to remain constant during the simulation, with the node locations varying but not their interconnections.

A single time step, from levels t^{k-1} and t^k to level t^{k+1}, is achieved without iteration as follows. First, boundary values of $\mathbf{v}^e$ at level k are computed and then interior values are computed from the elastic relations. This allows projection of the mesh positions:

$$\mathbf{x}_j^{k+1} = \mathbf{x}_j^{k-1} + 2\Delta t \mathbf{v}_j^e. \tag{24}$$

With $\mathbf{v}^e$ known we solve (21) for H^{k+1}. Then with $g\nabla\zeta^{k+1}$ known we solve (23) for $\mathbf{v}^{k+1}$. Since (23) is centred at $t^{k+1/2}$, we utilize $\mathbf{v}^e = (\mathbf{x}^{k+1} - \mathbf{x}^k)/\Delta t$ in this final calculation (Figure 1).

COMPARISON WITH ANALYTICAL SOLUTIONS

Numerical solutions of two one-dimensional moving boundary problems are compared with their corresponding analytical solutions. Both cases consider waves that propagate in a frictionless fluid ($\tau = 0$) toward a beach with a uniform slope α (Figure 2). It is convenient to express the

```
begin time step loop,  $k = 1 \ldots maxt$
    update time,  $t^k = t^{k-1} + \Delta t$
    calculate nodal bottom friction,  $\tau_j^k$
    calculate normal directions at moving boundary,  $\mathbf{n}_j^k$
    calculate new boundary location,  $\mathbf{x}_j^{k+1} \cdot \mathbf{n}_j^k = \mathbf{x}_j^{k-1} + 2\Delta t(\mathbf{v}_j^k \cdot \mathbf{n}_j^k)$
    apply known values of $\mathbf{x}_j^{k+1}$
    compute $\mathbf{x}^{k+1}$ for interior nodes
    calculate $\mathbf{v}_j^e$, $d\mathbf{v}_j^e/dt$ and $h_j^{k+1}$
    begin element loop for wave equation
        assemble stiffness matrix of the wave equation, $[A]^k$
        assemble wave equation right hand side, $\{RW\}^k$
    end element loop
    apply boundary conditions on fluid depth
    solve the wave equation
    update element velocity: $\mathbf{v}_j^e = \frac{\mathbf{x}_j^{k+1} - \mathbf{x}_j^k}{\Delta t}$
    begin element loop for momentum equation
        assemble momentum stiffness matrix, $[B]^k$
        assemble momentum right hand side, $\{RM\}^k$
    end element loop for momentum equation
    apply velocity boundary conditions
    solve the momentum equation to get velocities
    write results
    upate arrays in time,  $Z_j^{k-1} = Z_j^k$  and  $Z_j^k = Z_j^{k+1}$
end time step loop
```

Figure 1. Flow chart of algorithm. max$t$ is the maximum number of time steps, k indicates the current time level and j is a node index

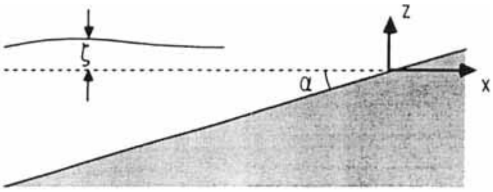

Figure 2. Definition sketch. The fluid has a boundary of uniform slope α and a free surface at height ζ above its undisturbed level

analytical solutions using the following dimensionless quantities: $\mathrm{z}=\zeta/\alpha L$, $\mathrm{u}=u/\surd(g\alpha L)$, $\mathrm{x}=x/L$, $\mathrm{t}=t\alpha g/L$, $\mathrm{c}^2=\mathrm{z}-\mathrm{x}$, $\lambda=2(\mathrm{u}+\mathrm{t})$ and $\sigma=4\mathrm{c}$. In these definitions the characteristic length L is specified for each problem.

First we consider an initial value problem in which the water level at the coastline is initially depressed. The fluid is held motionless and then released. The initial wave shape is given in parametric form in terms of the dimensionless sea surface elevation z and the dimensionless spatial co-ordinate x:

$$\mathrm{z}=\varepsilon\left(1-\frac{5}{2}\frac{a^3}{(a^2+\sigma^2)^{3/2}}+\frac{3}{2}\frac{a^5}{(a^2+\sigma^2)^{5/2}}\right), \tag{25a}$$

$$\mathrm{x}=-\frac{\sigma^2}{16}+\varepsilon\left(1-\frac{5}{2}\frac{a^3}{(a^2+\sigma^2)^{3/2}}+\frac{3}{2}\frac{a^5}{(a^2+\sigma^2)^{5/2}}\right). \tag{25b}$$

Here L corresponds to the initial length of the fluid domain and $a=1{\cdot}5(1+0{\cdot}9\varepsilon)^{1/2}$. These waves have maximum heights equal to ε and have heights equal to $0{\cdot}9\varepsilon$ at $\mathrm{x}=-1$. Furthermore, the slope of the sea surface at the shoreline is initially zero for such waves. The analytical solution is given by[20]

$$\mathrm{x}=-\frac{\mathrm{u}^2}{2}-\frac{a^2\sigma^2}{16}+\varepsilon\mathrm{Re}\left(1-2\frac{5/4-\mathrm{i}\lambda}{[(1-\mathrm{i}\lambda)^2+\sigma^2]^{3/2}}+\frac{3}{2}\frac{(1-\mathrm{i}\lambda)^2}{[(1-\mathrm{i}\lambda)^2+\sigma^2]^{5/2}}\right), \tag{26a}$$

$$\mathrm{t}=\tfrac{1}{2}a\lambda-\mathrm{u}, \tag{26b}$$

$$\mathrm{z}=\mathrm{x}+a^2\sigma^2/16, \tag{26c}$$

$$\mathrm{u}=\frac{8\varepsilon}{a}\mathrm{Im}\left(\frac{1}{[(1-\mathrm{i}\lambda)^2+\sigma^2]^{3/2}}-\frac{3}{4}\frac{1-\mathrm{i}\lambda}{[(1-\mathrm{i}\lambda)^2+\sigma^2]^{5/2}}\right). \tag{26d}$$

The motion of the shoreline is obtained from the same equations by setting $\sigma=0$. In applying the numerical solution technique, the domain is discretized on a grid which is initially 500 km and consists of 50 nodes. On the boundary located in deep water the fluid depth is specified according to the analytical solution and the other boundary is moving. The values of L and ε are 4166 km and 0·1 respectively. The simulation is carried out to 28·0 h using a time step of 0·1 h and the value of τ_0 used is 10^{-3}. The numerical solution shows good agreement with the analytical solution (Figure 3).

The next example considers the fluid motion induced by periodic forcing, such as by tides. The elevation of the free sea surface is prescribed at the fixed boundary:

$$\mathrm{z}=\varepsilon\cos(2\pi\mathrm{t}/\mathrm{T}). \tag{27}$$

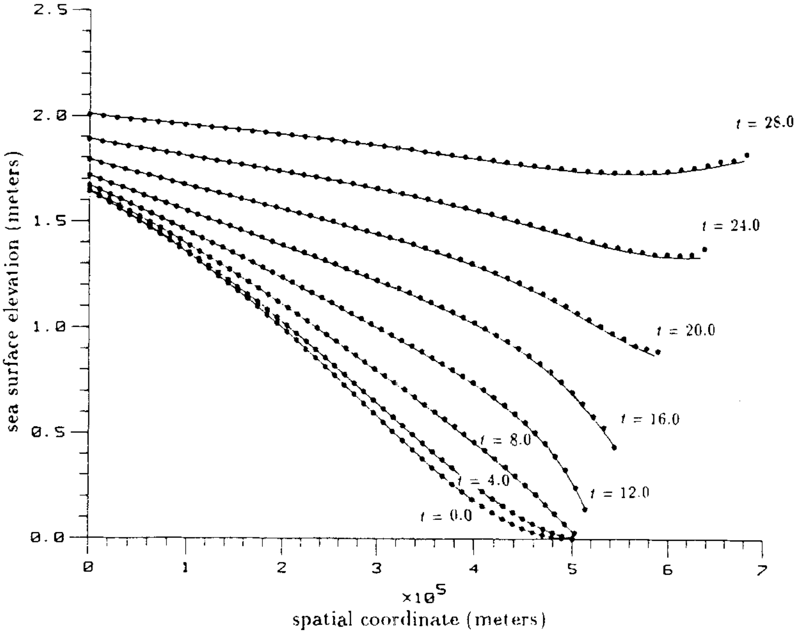

Figure 3. Time history of sea surface elevation for the initial value problem. The numerical solution (points) is compared with the analytical solution (solid curves). Time is given in hours

Here the scaled amplitude ε is related to the dimensional amplitude a by $\varepsilon = a/\alpha L$. The scaled period T is related to the dimensional period T by $\mathrm{T} = T\sqrt{(g\alpha/L)}$ and L is the total length of the undisturbed fluid domain. The analytical solution is presented by Carrier and Greenspan[20] and expressed in a simpler form by Johns:[21]*

$$\mathrm{z} = -\tfrac{1}{2}\mathrm{u}^2 + \mathrm{A}J_0(\pi\sigma/\mathrm{T})\cos(\pi\lambda/\mathrm{T}), \tag{28a}$$

$$\mathrm{u} = -\frac{\mathrm{A}J_1(\pi\sigma/\mathrm{T})}{\mathrm{c}}\sin\left(\frac{\pi\lambda}{\mathrm{T}}\right), \tag{28b}$$

where J_0 and J_1 denote Bessel functions of the first kind. The amplitude factor A is obtained by linearizing the governing equations on the fixed boundary:

$$\mathrm{A} = \varepsilon/J_0(4\pi/\mathrm{T}). \tag{29}$$

The displacement of the shoreline, ξ, is obtained from (28a) by setting $\sigma = 0$:

$$\xi = -\tfrac{1}{2}\mathrm{u}^2 + \mathrm{A}\cos(\pi\lambda/\mathrm{T}). \tag{30}$$

Specifically, we consider a wave which is forced with an amplitude of 0·1 m and a period of 12·4 h on the fixed boundary. The length of the undisturbed fluid domain is 100 km and it is

---

* In the work presented by Johns[21] a factor of four appears in front of the amplitude factor A in (28b). We find, however, that in order to satisfy the kinematic boundary condition on the moving boundary we need to discard this factor and apply the equations as presented in (28a) and (28b).

discretized on a grid consisting of 20 nodes. Here the numerical simulation is carried out for six forcing cycles using 124 time steps per cycle. The value of τ_0 is 10^{-3}. The solution is compared with the analytical solution at different points in time, with good agreement (Figure 4).

While the governing equations have approximately linear response when the fluid depth is large, we note that the solution close to the moving boundary is essentially non-linear in character. As the offshore tide propagates towards the shore, it becomes increasingly distorted

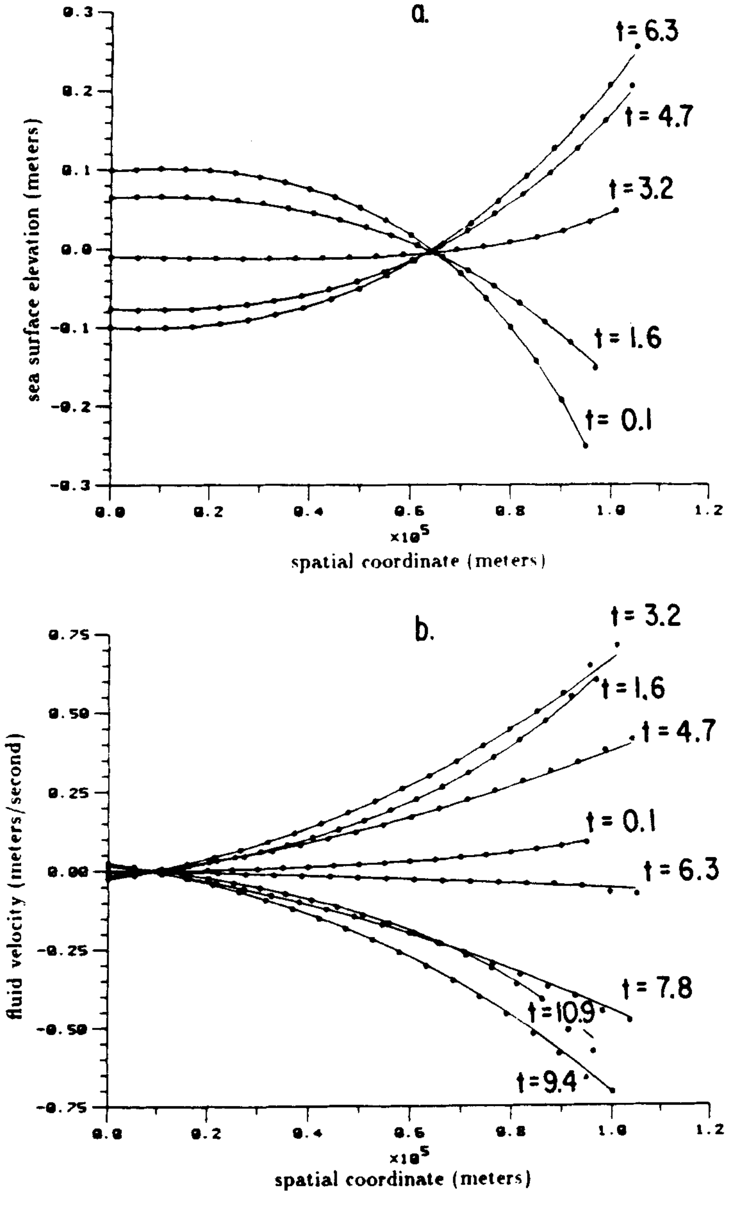

Figure 4. Time history of (a) sea surface elevation and (b) fluid velocities for the periodic problem. The numerical solution (points) is compared with the analytical solution (solid curves). Time is given in hours

due to increased influence of higher harmonics. This non-linear character of the governing equations puts high demands on the numerical solution technique, considering both stability and accuracy, under these limits. In Figures 5(a)–(d) the accuracy of the numerical solution is demonstrated for several constituents, and in Figure 6 the frequency spectrum of the numerical solution is compared with the analytical solution at a fixed point in the vicinity of the moving shoreline. The Fourier amplitude for the jth frequency, $A(j, x)$, is computed by the fast Fourier transform of the time series data for the first six periods of the simulation:

$$A(j, x)=\sum_{k=0}^{N-1} \zeta(k, x)\, \mathrm{e}^{\mathrm{i}2\pi jk/N}, \tag{31}$$

where k denotes the time level, i is the imaginary unit $\sqrt{(-1)}$ and N is the number of time levels. The numerical solution compares well with the analytical solution for each constituent. However, it also contains additional small-amplitude noise.

In addition, it should be mentioned that long-term stable numerical results have been obtained in the frictionless case. Experimentally we have found an unstable behaviour of the numerical solution for the periodic problem using $\tau_0=0$. Slowly growing wiggles in the solution eventually

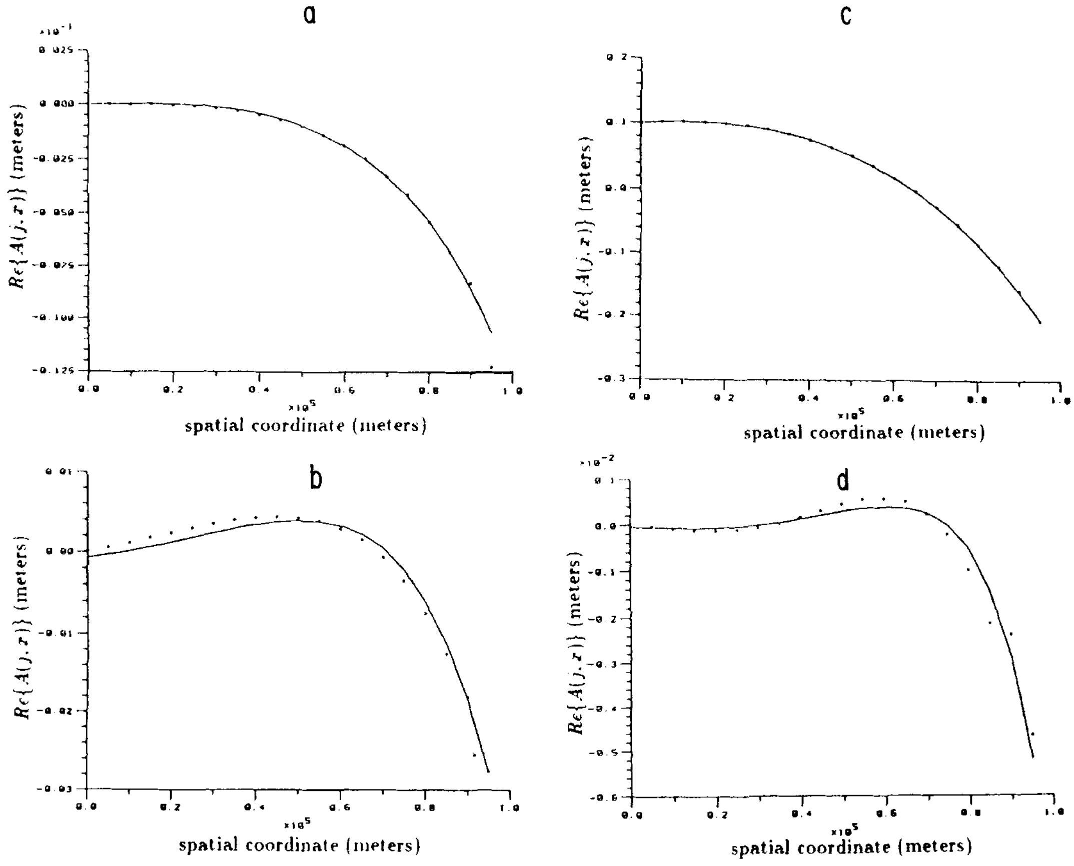

Figure 5. Four Fourier components of the decomposed sea surface elevation are shown as a function of the spatial coordinate. Re$\{A(j, x)\}$, is shown for the steady-state component (a), fundamental frequency (b), first harmonic (c) and second harmonic (d). The numerical solution (points) is compared with the analytical solution (solid curves)

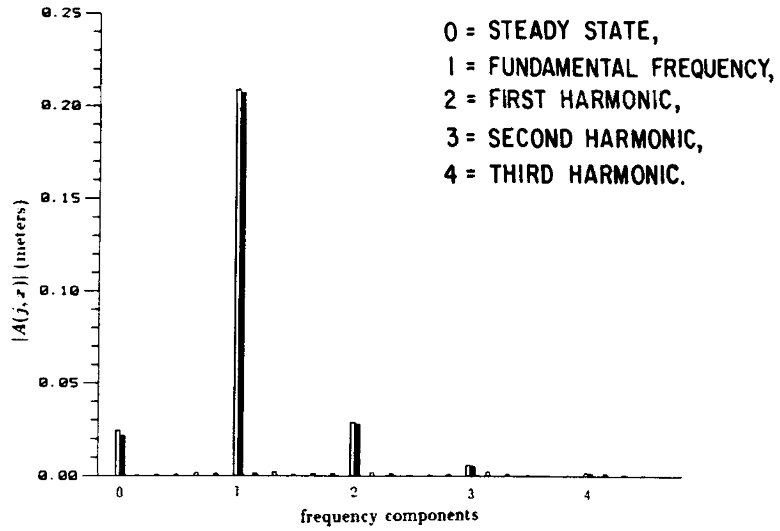

Figure 6. Comparison of the numerical solution versus the analytical solution in the frequency domain. $|A(j, x_0)|$ is shown for $j = 0$ to 28 for the numerical solution (white bars) and compared with the analytical solution (shaded bars) at a fixed point x_0 in the vicinity of the shoreline

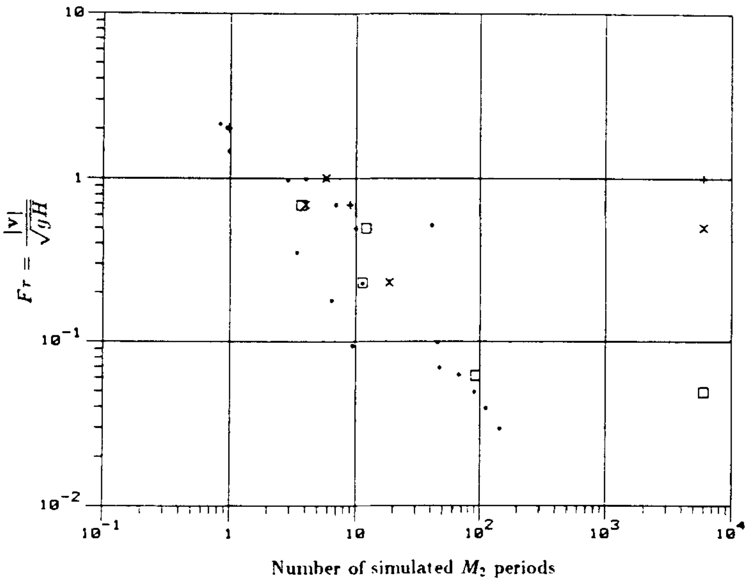

Figure 7. Experimental results in the frictionless periodic case showing the influence of Fr and τ_0 on the stability. The time until negative fluid depth is encountered in the solution is shown as a function of Fr for $\tau_0 = 10^{-4}\,\mathrm{s}^{-1}$ ('+' signs), $\tau_0 = 10^{-5}\,\mathrm{s}^{-1}$ ('×' signs), $\tau_0 = 10^{-6}\,\mathrm{s}^{-1}$ (squares) and $\tau_0 = 0\,\mathrm{s}^{-1}$ (points)

render negative fluid depth, which is chosen to be the criterion for terminating the program. We have found the termination time being related to the Froude number:

$$Fr = |\mathbf{v}|/\sqrt{(gH)}. \tag{32}$$

The maximum Fr is reported in each case, computed by using the average of H and $|\mathbf{v}|$ on each element. By using $\tau_0 > 0$ we can obtain long-term stable numerical results (Figure 7). However, it is to be noted that by severely increasing τ_0 ($\tau_0 \gg \omega$, where ω is the fundamental frequency) the wave equation reduces to the primitive continuity equation, at which point we expect to encounter problems which have been discussed earlier.[11]

NUMERICAL TEST CASES

Two test cases with relatively large boundary excursions are presented. The geometries are idealized while still representing problems of physical significance. The forcing is periodic, corresponding to the M_2 tide, which has a period of 12·4 h. The Coriolis and wind stress effects are neglected. Further, the value of the bottom friction parameter τ is assumed constant and equal to τ_0 ($10^{-4}\ \mathrm{s}^{-1}$). The simulation time corresponds to six M_2 periods using 124 time steps per period.

In the first example a rectangular domain with uniformly sloping bathymetry is considered. The basin has dimensions 10 km by 10 km and a maximum bathymetry of 1 m at the forcing boundary (Figure 8). The grid consists of 49 nodes and 72 elements. The tidal amplitude at the

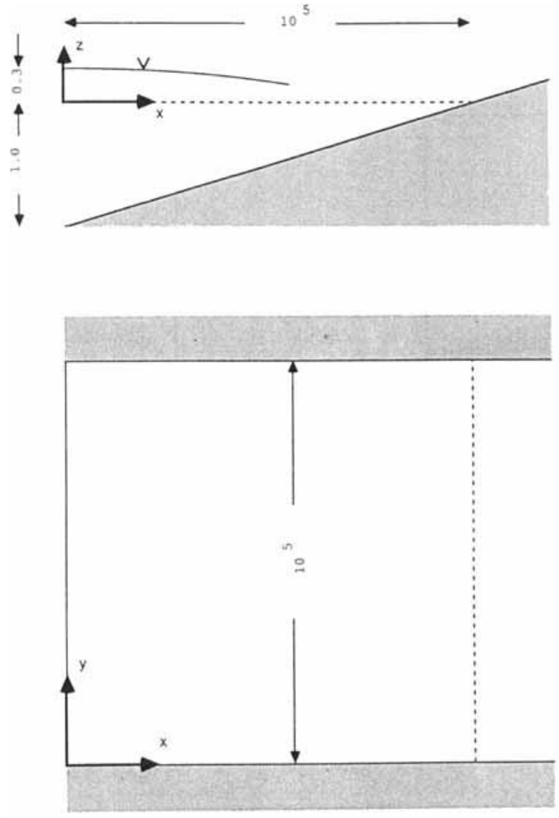

Figure 8. Definition sketch of rectangular basin. The tidal flow in a rectangular domain is studied. The forcing boundary is located at $x = 0$, on which a sinusoidally varying sea surface elevation is prescribed. The dashed line shows the location of the moving boundary at rest. There is no flux of water across the boundaries shown as thick shaded bands. Lengths are given in metres

forcing boundary is 0·3 m, producing a maximum boundary deformation of approximately 50% of the domain (Figure 9). The wavelength of the fundamental frequency is considerably larger than the fluid domain, which results in a relatively uniform flow field (Figure 10). In Figure 11 the boundary location is shown as a function of time.

In the second case an L-shaped basin is studied which has a length of 30 km and a width of 50 km. The bathymetry has a maximum of 1·0 m and a uniform slope (Figure 12). Here the tidal amplitude at the forcing boundary is 0·1 m, creating a boundary motion with an approximate range of 6Δx, where Δx is the mesh spacing (Figure 13). The grid consists of 923 nodes and 1708 elements. In Figure 14 the boundary location is shown at different points in time. In Figures 15 and 16 the solutions for **v** and H are shown at $t = 56{\cdot}0$ h. The tidal distortion is shown in Figure 17 in terms of time series plots of the boundary location for several points along the boundary.

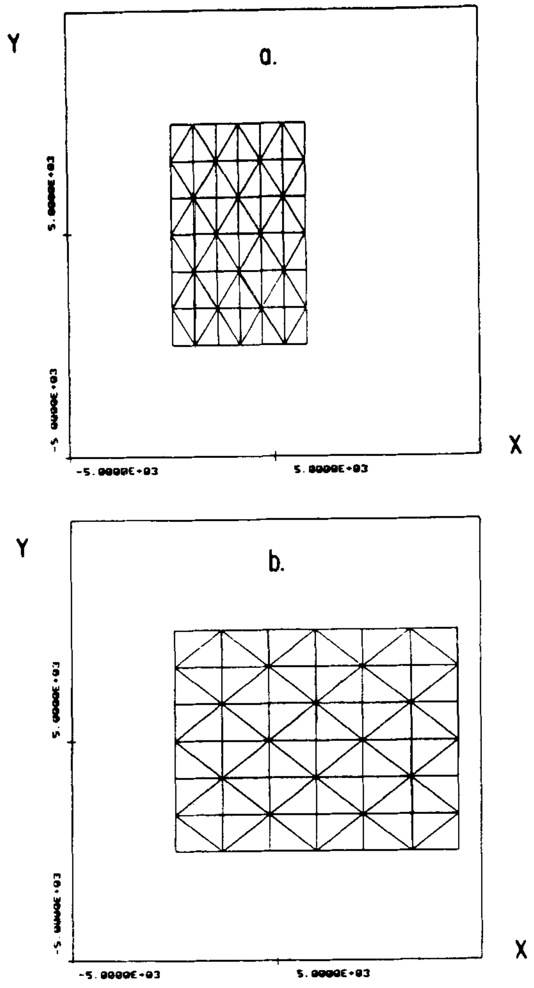

Figure 9. Maximum deformation of the rectangular mesh. The grid for the rectangular domain is shown at (a) $t = 58{\cdot}6$ h and (b) $t = 65{\cdot}6$ h

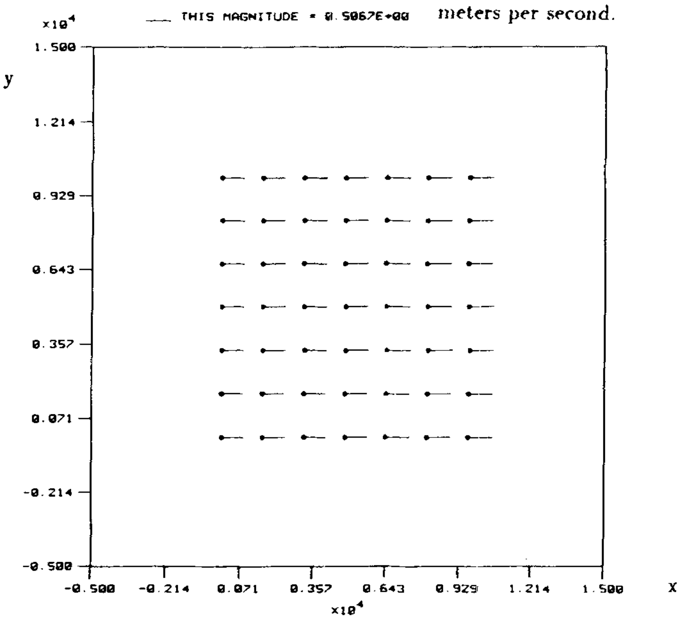

Figure 10. Vector plot of fluid velocities in the rectangular case. The nodal values of the fluid velocitiy are shown at $t=62{\cdot}3$ h

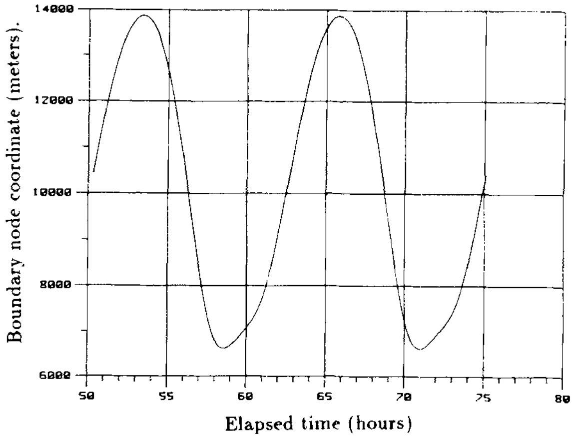

Figure 11. Time series plot of boundary location for rectangular case. The motion in the x-direction is shown for the boundary node located halfway between the fixed boundaries

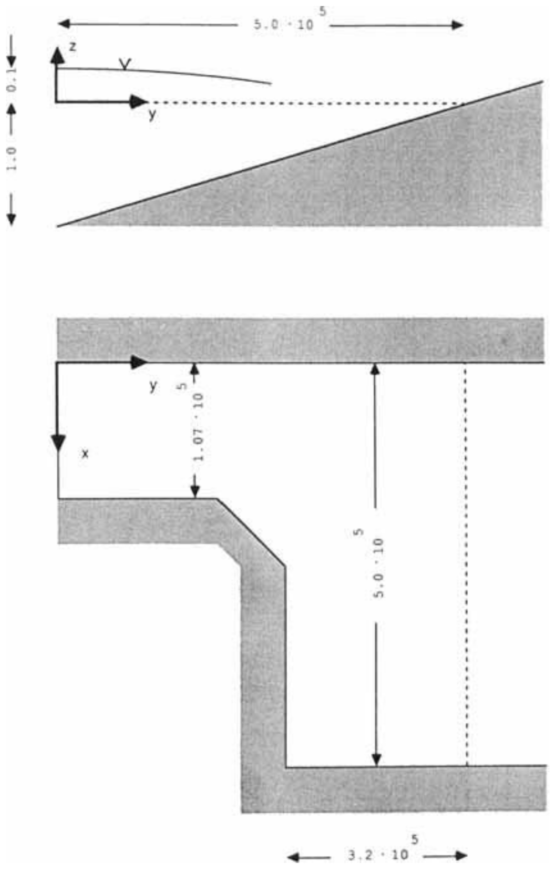

Figure 12. Definition sketch for the L-shaped domain. The tidal flow in an L-shaped domain is studied. The forcing boundary is located at $y=0$, on which a sinusoidally varying sea surface elevation is prescribed. The dashed line shows the location of the moving boundary at rest. There is no flux of water across the boundaries shown as thick shaded bands. Lengths are given in metres

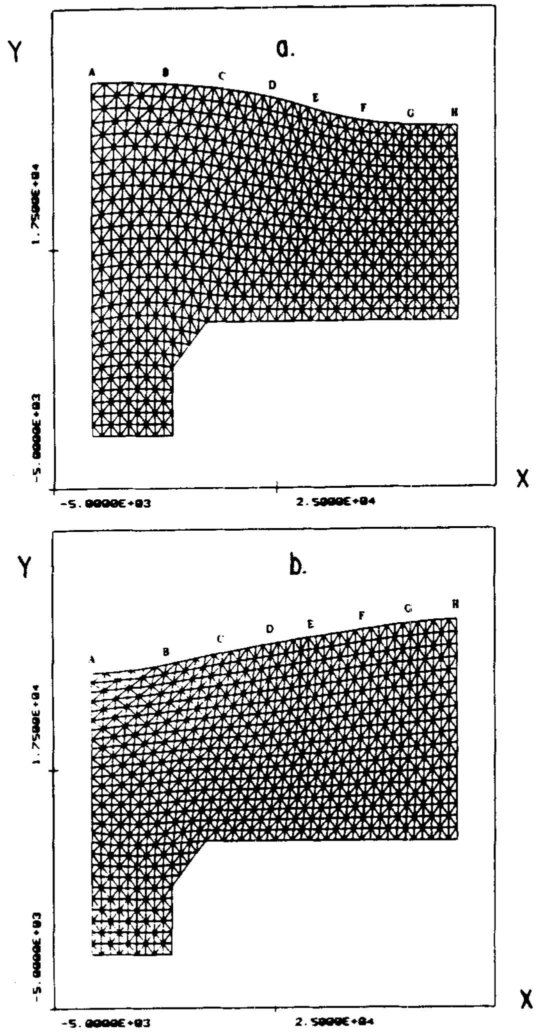

Figure 13. Maximum deformation of the grid in the L-shaped case. The mesh for the L-shaped domain is shown at (a) $t = 57{\cdot}0$ h and (b) $t = 63{\cdot}0$ h

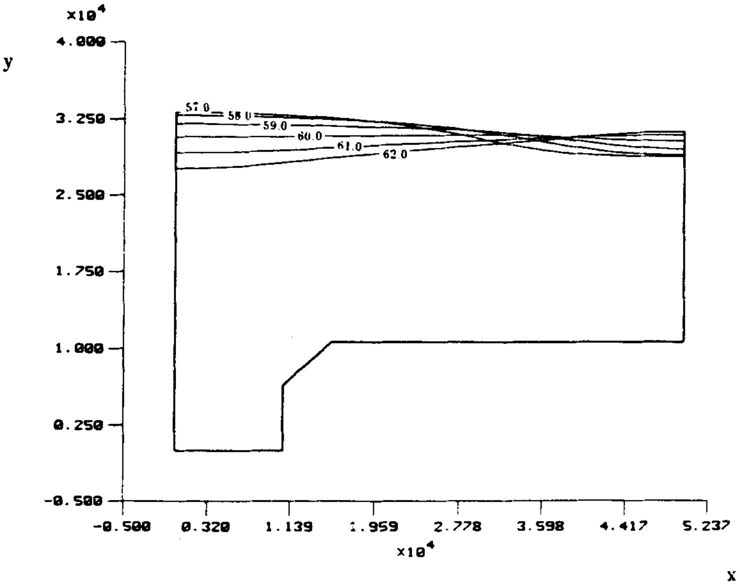

Figure 14. Time history of boundary location in the L-shaped case. The location of the boundary is shown at different points in time (hours)

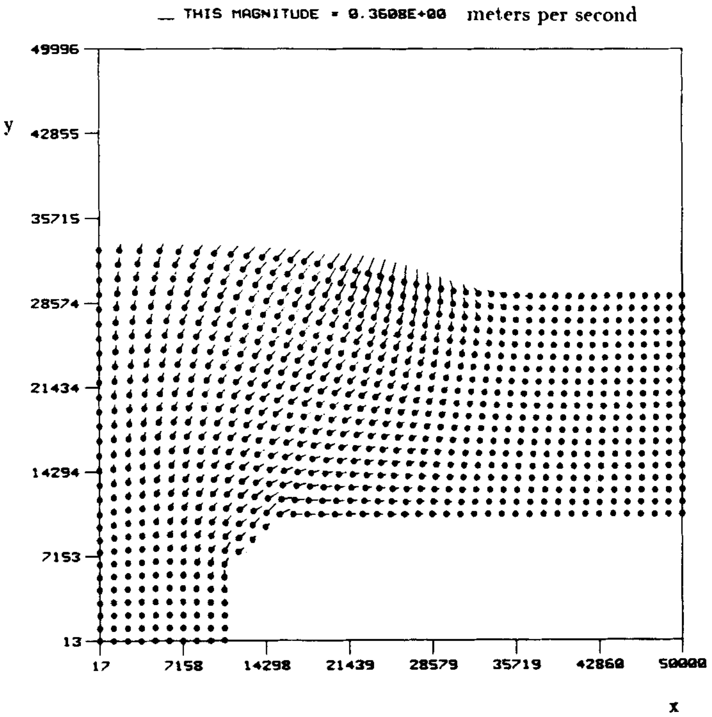

Figure 15. Vector plot of fluid velocities in the L-shaped case. The nodal values of the fluid velocity are shown at $t = 56{\cdot}0$ h

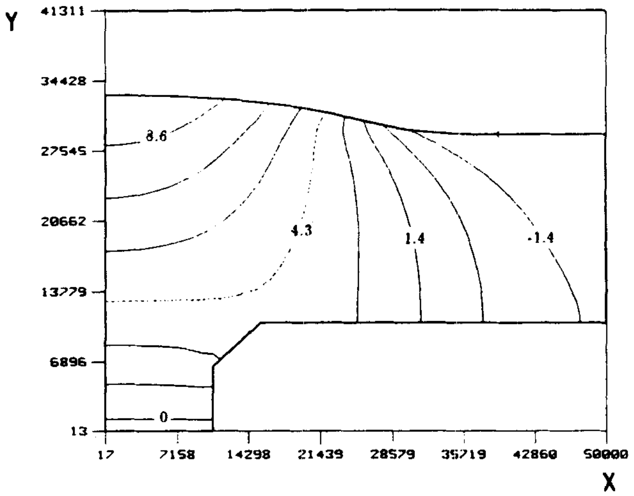

Figure 16. Sea surface elevation in the L-shaped case. Free surface elevation contours (centimetres) are shown at $t = 56{\cdot}0$ h

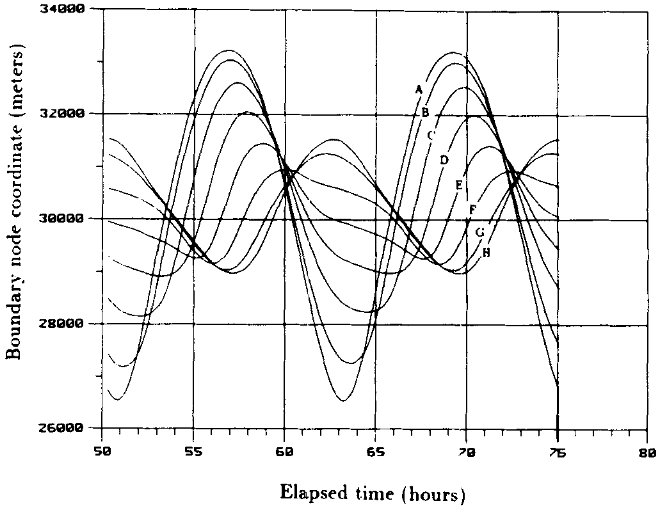

Figure 17. Time series plot of boundary location for the L-shaped case. The motion of the boundary in the y-direction is shown at several points along the boundary. Labels correspond to locations defined in Figures 13(a) and (b)

DISCUSSION

The weak form of the shallow water wave equation proposed here has several desirable features:

(a) For fixed boundary problems ($\mathbf{v}^e \equiv 0$) it reduces to the form presently being used, whose properties are reasonably well understood.

(b) Since only first derivatives in space are involved, it may be implemented on the simplest finite elements.

(c) The natural conditions on the moving boundary are invoked.

Implementation on linear triangles with a conventional three-level, semi-implicit time-stepping algorithm shows satisfying results. The retention of a lossless analytic solution over several tidal periods is especially noteworthy.

Two numerical strategies have been used without attempting to maximize their cost-effectiveness: the interior gridding and the treatment of the advective terms. These features together dominate the run time—some of the 2D cases require tens of hours of CPU time on a VaxStation II. Our experience has shown that the elastic gridding is generally very robust among mapping strategies; at the same time it is the most expensive, since all boundary displacements contribute directly to all interior node displacements, and x- and y-displacements are intimately coupled. In these applications simpler methods may well prove to be entirely adequate. Transfinite mappings are a particularly attractive candidate.[22] Relative to the advective terms, we look forward to future advances and expect that algorithmic improvements in the fixed mesh reduction of this problem will be applicable as well in the more general context of moving boundary problems.

ACKNOWLEDGEMENTS

This work was supported by the National Science Foundation, Grant #CEE-8352226, and by the Digital Equipment Corporation. We thank Dr. David G. Aubrey of the Woods Hole Oceanographic Institution for several discussions early in the project, and Prof. Francisco Werner of Dartmouth for guidance along the way.

APPENDIX

Proof

$$\frac{\mathrm{d}}{\mathrm{d}t}\nabla A=\nabla\frac{\mathrm{d}A}{\mathrm{d}t}-\nabla\mathbf{v}^{\mathrm{e}}\cdot\nabla A, \tag{33}$$

where A is a scalar quantity. The left-hand side is equal to

$$\begin{aligned}
&\frac{\mathrm{d}}{\mathrm{d}t}\left[\frac{\partial A}{\partial x}\hat{\mathbf{x}}+\frac{\partial A}{\partial y}\hat{\mathbf{y}}\right]\\
&\quad=\frac{\partial}{\partial t}\left[\frac{\partial A}{\partial x}\hat{\mathbf{x}}+\frac{\partial A}{\partial y}\hat{\mathbf{y}}\right]+u^{\mathrm{e}}\frac{\partial}{\partial x}\left[\frac{\partial A}{\partial x}\hat{\mathbf{x}}+\frac{\partial A}{\partial y}\hat{\mathbf{y}}\right]+v^{\mathrm{e}}\frac{\partial}{\partial y}\left[\frac{\partial A}{\partial x}\hat{\mathbf{x}}+\frac{\partial A}{\partial y}\hat{\mathbf{y}}\right]\\
&\quad=\frac{\partial}{\partial x}\left[\frac{\partial A}{\partial t}\right]\hat{\mathbf{x}}+\frac{\partial}{\partial y}\left[\frac{\partial A}{\partial t}\right]\hat{\mathbf{y}}+u^{\mathrm{e}}\frac{\partial^2 A}{\partial x^2}\hat{\mathbf{x}}+u^{\mathrm{e}}\frac{\partial^2 A}{\partial x\partial y}\hat{\mathbf{y}}+v^{\mathrm{e}}\frac{\partial^2 A}{\partial x\partial y}\hat{\mathbf{x}}+v^{\mathrm{e}}\frac{\partial^2 A}{\partial y^2}\hat{\mathbf{y}}\\
&\quad=\frac{\partial}{\partial x}\left[\frac{\mathrm{d}A}{\mathrm{d}t}\right]\hat{\mathbf{x}}+\frac{\partial}{\partial y}\left[\frac{\mathrm{d}A}{\mathrm{d}t}\right]\hat{\mathbf{y}}-\frac{\partial}{\partial x}\left[u^{\mathrm{e}}\frac{\partial A}{\partial x}+v^{\mathrm{e}}\frac{\partial A}{\partial y}\right]\hat{\mathbf{x}}-\frac{\partial}{\partial y}\left[u^{\mathrm{e}}\frac{\partial A}{\partial x}+v^{\mathrm{e}}\frac{\partial A}{\partial y}\right]\hat{\mathbf{y}}\\
&\qquad+u^{\mathrm{e}}\frac{\partial^2 A}{\partial x^2}\hat{\mathbf{x}}+u^{\mathrm{e}}\frac{\partial^2 A}{\partial x\partial y}\hat{\mathbf{y}}+v^{\mathrm{e}}\frac{\partial^2 A}{\partial x\partial y}\hat{\mathbf{x}}+v^{\mathrm{e}}\frac{\partial^2 A}{\partial y^2}\hat{\mathbf{y}}\\
&\quad=\frac{\partial}{\partial x}\left[\frac{\mathrm{d}A}{\mathrm{d}t}\right]\hat{\mathbf{x}}+\frac{\partial}{\partial y}\left[\frac{\mathrm{d}A}{\mathrm{d}t}\right]\hat{\mathbf{y}}-\left[\frac{\partial u^{\mathrm{e}}}{\partial x}\frac{\partial A}{\partial x}+\frac{\partial v^{\mathrm{e}}}{\partial x}\frac{\partial A}{\partial y}\right]\hat{\mathbf{x}}-\left[\frac{\partial u^{\mathrm{e}}}{\partial y}\frac{\partial A}{\partial x}+\frac{\partial v^{\mathrm{e}}}{\partial y}\frac{\partial A}{\partial y}\right]\hat{\mathbf{y}}\\
&\quad=\nabla\frac{\mathrm{d}A}{\mathrm{d}t}-\nabla\mathbf{v}^{\mathrm{e}}\cdot\nabla A,
\end{aligned}$$

which is equal to the right-hand side. Above, $\hat{\mathbf{x}}$ and $\hat{\mathbf{y}}$ are unit vectors in the **x**- and **y**-directions.

Proof

$$\frac{\mathrm{d}}{\mathrm{d}t}\nabla\cdot\mathbf{B}=\nabla\cdot\frac{\mathrm{d}\mathbf{B}}{\mathrm{d}t}-\nabla\mathbf{v}^{\mathrm{e}}:\nabla\mathbf{B}, \tag{34}$$

where **B** is a vector quantity with x- and y-components B_x and B_y. The left-hand side is equal to

$$\begin{aligned}
\frac{\mathrm{d}}{\mathrm{d}t}\left[\frac{\partial B_x}{\partial x}+\frac{\partial B_y}{\partial y}\right]
&=\frac{\partial}{\partial t}\left[\frac{\partial B_x}{\partial x}+\frac{\partial B_y}{\partial y}\right]+u^{\mathrm{e}}\frac{\partial}{\partial x}\left[\frac{\partial B_x}{\partial x}+\frac{\partial B_y}{\partial y}\right]+v^{\mathrm{e}}\frac{\partial}{\partial y}\left[\frac{\partial B_x}{\partial x}+\frac{\partial B_y}{\partial y}\right]\\
&=\frac{\partial}{\partial x}\left[\frac{\partial B_x}{\partial t}\right]+\frac{\partial}{\partial y}\left[\frac{\partial B_y}{\partial t}\right]+u^{\mathrm{e}}\frac{\partial^2 B_x}{\partial x^2}+u^{\mathrm{e}}\frac{\partial^2 B_y}{\partial x\partial y}+v^{\mathrm{e}}\frac{\partial^2 B_x}{\partial x\partial y}+v^{\mathrm{e}}\frac{\partial^2 B_y}{\partial y^2}\\
&=\frac{\partial}{\partial x}\left[\frac{\mathrm{d}B_x}{\mathrm{d}t}\right]+\frac{\partial}{\partial y}\left[\frac{\mathrm{d}B_y}{\mathrm{d}t}\right]-\frac{\partial}{\partial x}\left[u^{\mathrm{e}}\frac{\partial B_x}{\partial x}+v^{\mathrm{e}}\frac{\partial B_x}{\partial y}\right]-\frac{\partial}{\partial y}\left[u^{\mathrm{e}}\frac{\partial B_y}{\partial x}+v^{\mathrm{e}}\frac{\partial B_y}{\partial y}\right]\\
&\qquad+u^{\mathrm{e}}\frac{\partial^2 B_x}{\partial x^2}+u^{\mathrm{e}}\frac{\partial^2 B_y}{\partial x\partial y}+v^{\mathrm{e}}\frac{\partial^2 B_x}{\partial x\partial y}+v^{\mathrm{e}}\frac{\partial^2 B_y}{\partial y^2}\\
&=\frac{\partial}{\partial x}\left[\frac{\mathrm{d}B_x}{\mathrm{d}t}\right]+\frac{\partial}{\partial y}\left[\frac{\mathrm{d}B_y}{\mathrm{d}t}\right]-\frac{\partial u^{\mathrm{e}}}{\partial x}\frac{\partial B_x}{\partial x}-\frac{\partial v^{\mathrm{e}}}{\partial x}\frac{\partial B_x}{\partial y}-\frac{\partial u^{\mathrm{e}}}{\partial y}\frac{\partial B_y}{\partial x}-\frac{\partial v^{\mathrm{e}}}{\partial y}\frac{\partial B_y}{\partial y}\\
&=\nabla\cdot\frac{\mathrm{d}\mathbf{B}}{\mathrm{d}t}-\nabla\mathbf{v}^{\mathrm{e}}:\nabla\mathbf{B},
\end{aligned}$$

which is equal to the right-hand side.

REFERENCES

1. D. R. Lynch and W. G. Gray, 'Finite element simulation of flow in deforming regions', *J. Comput. Phys.*, **36,** 135–153 (1980).
2. D. R. Lynch and K. O'Neill, 'Continuously deforming finite elements for the solution of parabolic problems with and without phase change', *Int. j. numer. methods eng.*, **17,** 81–96 (1981).
3. D. R. Lynch, 'Unified approach to simulation on deforming elements with applications to phase change problems', *J. Comput. Phys.*, **47,** 387–411 (1982).
4. J. M. Sullivan, D. R. Lynch and K. O'Neill, 'Finite element simulation of planar instabilities during solidification of an undercooled melt', *J. Comput. Phys.*, **69,** 81–111 (1987).
5. J. M. Sullivan and D. R. Lynch, 'Non-linear simulation of dendritic solidification of an undercooled melt', *Int. j. numer. methods eng.*, in press (1988).
6. R. J. Gelinas, S. K. Doss and K. Miller, 'The moving finite element method: applications to general partial differential equations with multiple large gradients', *J. Comput. Phys.*, **40,** 202–249 (1981).
7. H. S. Kheshgi and L. E. Scriven, 'Penalty finite element analysis of unsteady free surface flows', in R. H. Gallagher *et al.* (eds), *Finive Element in Fluids, Vol. 5*, Wiley, New York, 1983.
8. E. C. Hume III, R. A. Brown and W. M. Deen, 'Comparison of boundary and finite element methods for moving boundary problems governed by a potential', *Int. j. numer. methods eng.*, **21,** 1295–1314 (1985).
9. L. H. Ungar, N. Ramprasad and R. A. Brown, 'Finite element methods for unsteady solidification problems arising in prediction of morphological structure', *J. Sci. Comput.*, in press (1988).
10. E. M. Ronquist and A. T. Patera, 'A Legendre spectral element method for the Stefan problem', *Int. j. numer. methods. eng.*, **24,** 2273–2299 (1987).
11. D. R. Lynch and W. G. Gray, 'A wave equation model for finite element tidal computations', *Comput. Fluids*, **7,** 207–228 (1979).
12. I. P. E. Kinnmark and W. G. Gray, 'Time weighting of the momentum equation in explicit wave equation models of

surface water flow', K.-P. Holz *et al.* (eds), *Proc. 4th Int. Conf. on Finite Elements in Water Resources*, Springer-Verlag, Berlin, 1982, pp. 5.67–5.77.

13. I. P. E. Kinnmark and W. G. Gray, 'A generalized wave equation formulation of tidal circulation', in C. Taylor *et al.* (eds), *Proc. 4th Int. Conf. on Numerical Methods in Laminar and Turbulent Flows*, Pineridge Press, Swansea, 1985, pp. 1312–1324.
14. I. P. E. Kinnmark, 'The shallow water equations: formulation, analysis and application', in C. A. Brebbia and S. A. Orszag (eds), *Lecture Notes in Engineering, Vol. 15*, Springer-Verlag, Berlin, 1985.
15. W. G. Gray, J. Drolet and I. P. E. Kinnmark, 'A simulation of tidal flow in the southern part of the North Sea and the English Channel', *Adv. Water Resources*, **10**, 131–137 (1987).
16. F. E. Werner and D. R. Lynch, 'Field studies with the wave equation formulation', *Proc. 6th Int. Conf. on Finite Elements in Water Resources*, Lisbon, 1986.
17. F. E. Werner and D. R. Lynch, 'Field verification of wave equation tidal dynamics in the English Channel and southern North Sea', *Adv. Water Resources*, **10**, 115–130 (1987).
18. D. R. Lynch and F. E. Werner, 'Long-term simulation and harmonic analysis of North Sea English Channel tides', *Proc. VII Int'l Conf. on Comp. Meths in Water Resources*, M. A. Celia *et al.* (eds), Computational Mechanics Publications, Southampton, June 1988.
19. F. W. Wubs, 'Stabilization of explicit methods for hyperbolic partial differential equations', *Int. j. numer. methods fluids*, **6**, 641–657 (1986).
20. G. F. Carrier and H. P. Greenspan, 'Water waves of finite amplitude on a sloping beach', *J. Fluid Mech.*, **4**, 97–109 (1958).
21. B. Johns, 'Numerical integration of the shallow water equations over a sloping shelf', *Int. j. numer. methods fluids*, **2**, 253–261 (1982).
22. M. R. Albert and K. O'Neill, 'The use of transfinite mappings with finite elements on a moving mesh for two-dimensional phase change', in *Adaptive Computational Methods for Partial Differential Equations*, SIAM, Philadelphia, 1983.